Chemical Geology 719 (2026) 123550

Contents lists available at ScienceDirect

Chemical Geology

journal homepage: www.elsevier.com/locate/chemgeo

pH-dependent uptake and secondary Phases Formation of rare earth elements (REE) on Kaolinite

Hang Xu [a], Johannes Leisen [b], Yinghao Wen [a], Yixuan Yang [a], Pan Liu [a], Yuanzhi Tang [a,*]

[a] School of Earth and Atmospheric Sciences, Georgia Institute of Technology, 311 Ferst Drive, Atlanta, GA 30332-0340, United States
[b] School of Chemistry and Biochemistry, Georgia Institute of Technology, 311 Ferst Drive, Atlanta, GA 30332-0340, United States

ARTICLE INFO

Editor: Karen Johannesson

Keywords:
REE occurrences
Phosphate
Secondary chemical weathering
Nuclear magnetic resonance
X-ray absorption spectroscopy

ABSTRACT

Rare earth elements (REE) are indispensable to advanced and clean energy technologies. In response to the rising demand for REE, a comprehensive understanding of their occurrence and transport in natural environments is highly desired for the prediction and identification of potential REE resources. Recent studies have identified phosphate as a key natural ligand that influences REE behaviors during weathering and the formation of REE-phosphate minerals, one major type of natural REE resource. Although pH was found to strongly affect the sorption behaviors of REE and phosphate onto clay minerals, a molecular-level understanding of the reaction mechanisms remains lacking. Here, we elucidate the local coordination environment and molecular level reaction mechanisms of REE and phosphate on kaolinite at different pH condition using solid-state nuclear magnetic resonance (NMR) and synchrotron X-ray absorption spectroscopy (XAS). The results show that pH dictates the occurrence of multiple reactions, including solution coprecipitation, selective sorption coupled with surface coprecipitation, and competitive sorption accompanied by surface complexation. Moreover, pH strongly affects the crystallinity of the resulting REE-phosphate surface precipitates. These findings highlight the importance of pH alteration and ligand availability in dictating REE speciation and mobility during weathering processes and provide new insights into the underlying reaction pathways that govern REE occurrences and transport in the natural environments.

1. Introduction

Rare earth elements (REE) include the 15 lanthanides, yttrium (Y), and scandium (Sc). Their unique electronic configurations and associated optical, magnetic, and catalytic properties make them indispensable for many advanced industrial and military technologies (Hossain et al., 2021; Hughes et al., 2007; Ryoo et al., 2020). REE can be produced from the processing of natural REE ore deposits (Balaram, 2019; Li et al., 2022) and the recycling from non-conventional feedstocks such as spent batteries, coal fly ash, and municipal solid waste incineration ash (Liu et al., 2023; Porvali et al., 2018; Wen et al., 2023). With the geopolitical constraints with global REE supply, discovering and securing alternative REE resources is a strategic priority for many countries (Barteková and Kemp, 2016). Therefore, understanding the geochemical pathways governing REE mobility, transport, and fractionation in various enriched natural settings is essential for resources exploration, efficient extraction and recovery, and downstream processing.

Clay-hosted ion-adsorption deposits (IADs), phosphorite deposits (REE-phosphate mineral hosted), and carbonatites (REE-carbonate mineral hosted) are among the most important natural REE resources (Borst et al., 2020a; Emsbo et al., 2016; Van Gosen et al., 2019). These deposits form and evolve through series of geological processes such as magmatism, hydrothermal circulation, metamorphism, secondary weathering, and erosion (Benson and Watts, 2024; Elliott et al., 2018; Jaireth et al., 2014; Louvel et al., 2022; Sanematsu and Watanabe, 2016), which are crucial in shaping distinct REE distribution patterns. Magmatic and hydrothermal processes imprint the parent-rock inheritances and the original REE signatures, whereas subsequent weathering extensively modifies the present-day deposit profiles (Elliott et al., 2018). Secondary weathering, in particular, is a defining process in many economically significant REE deposits worldwide, generating lateritic regolith and ore bodies that have undergone intense weathering coupled with complex geochemical reactions (Hutchinson et al., 2022; Li et al., 2019). Key geochemical factors (e.g., solution chemistry, ligand presence/availability, and mineral substrates) control REE sorption,

* Corresponding author.
E-mail address: yuanzhi.tang@eas.gatech.eduyuanzhi.tang (Y. Tang).

https://doi.org/10.1016/j.chemgeo.2026.123550
Received 1 April 2026; Received in revised form 23 May 2026; Accepted 27 May 2026
Available online 28 May 2026

dissolution, reprecipitation, and nucleation (Boxleiter and Elliott, 2023; Elliott et al., 2018; Tang and Johannesson, 2010). Consequently, the underlying geochemical mechanisms operating under these various constraints have received increasing attention in recent years; however, most studies are field-based, and the molecular-scale reactions underlying these observations remain poorly understood.

Our recent study demonstrated the effects of phosphate on REE sorption at the kaolinite-water interfaces, suggesting the distinct sorption behaviors of REE and phosphate on clay minerals are strongly pH-dependent (Xu et al., 2025). Field studies also highlight the key role of pH in weathered horizons, where REEs released from mineral decomposition migrate downward and are subsequently adsorbed onto clay minerals or incorporated into secondary phases in deeper layers, particularly under favorable pH conditions (Wu et al., 2023). In REE-enriched regolith such as IADs, pH commonly increases from ~4 at the surface to ~6.5 in the enriched subsurface layers (Huang et al., 2021a; Pan et al., 2024; Wu et al., 2023). The depletion of REE in the upper horizons and their enrichment at depth, along with the pH alteration, indicate the crucial role of pH in controlling REE mobility.

While IADs in East Asia have received extensive attention and account for more than 80% of the global supply of mined heavy REEs, similar REE enrichment has also been identified in the southeastern United States, particularly within the Piedmont Province and Upper Coastal Plain, but remain comparatively underexplored. Both deposit types developed from granitic parent materials under highly weathered conditions (Boxleiter et al., 2024). However, unlike IADs in East Asia, where ion-exchangeable REEs dominate, kaolin-hosted deposits in the southeastern United States additionally contain substantial secondary REE-bearing phosphate minerals alongside ion-exchangeable REEs (Cheshire et al., 2018; Boxleiter et al., 2026). Previous field studies also highlighted the positive correlation between REE and phosphate concentrations within these deposits (Boxleiter et al., 2024). These observations raise important questions about the formation pathways of secondary mineral phases and suggest that phosphate may play a key role in controlling REE behavior during the development of kaolinite-rich strata in the southeastern United States, with implications for regional domestic REE supply chains. Meanwhile, although ion-exchangeable pathways dominates in classic IADs, especially those in East Asia, REE-phosphate minerals have also been observed in some deposits (Boxleiter et al., 2026). It suggests that REE-phosphate interactions may still co-occur locally in microsites where phosphate is released through primary mineral dissolution, biogenetic input, or organic matter decomposition, further highlighting the role of phosphate in dictating REE behaviors in clay-associated systems. In addition, both kaolin deposits in the southeastern United States and classic IADs exhibit spatial variability in porewater pH, with more acidic conditions in organic-rich zones due to organic acid production and relatively more neutral conditions in organic-lean units (Boxleiter et al., 2024). While these field observations reveal pH variability in REE deposits, its role in controlling REE accumulation and phase formation, as well as the underlying interfacial mechanisms at the microscale, remain poorly understood.

To address these knowledge gaps, this study aims to systematically investigate the sorption behaviors of REE and phosphate onto kaolinite across a wide pH range, expecting to establish a broader framework for the prediction and identification of REE behaviors, and to define the mechanistic boundaries among distinct interfacial reaction pathways under pH fluctuations or transient geochemical gradients during weathering processes. We also elucidate the molecular-level dynamics of REE local coordination and identify the formation of secondary REE-phases. Kaolinite was selected as a representative clay mineral common in weathering environments and in REE deposits such as IADs and mined kaolin ores (Borst et al., 2020a; Huang et al., 2021b; Li et al., 2019; Wu et al., 2023). Yttrium (Y) was used as the a probe of REE, and phosphate (P) was selected as an inorganic ligand because it is prevalent in various natural systems (soils, sediments, marine, etc) and is associated with one of the most important REE resources (i.e., REE-phosphate minerals) (Balaram, 2019; Jackson and Williams, 1985). Batch sequential sorption experiments were conducted to simulate the selective uptake of Y and P by kaolinite, thereby reproducing their natural occurrence and sorption sequences. One-dimension ^{31}P nuclear magnetic resonance (^{31}P NMR) was applied to characterize phosphate speciation. ^{31}P/^{27}Al Rotational Echo Adiabatic Passage Double Resonance (REAPDOR) NMR supported by SPINEVOLUTION numerical simulation was performed to resolve phosphate local bonding environments and interfacial structures. Synchrotron X-ray absorption spectroscopy (XAS) was performed to examine the local coordination of Y during a series of interfacial reactions. Collectively, results from sequential sorption experiments and complementary analytical techniques provide a mechanistic foundation for interpreting REE behaviors in diverse natural reservoirs and for linking macroscopic REE distribution to the underlying microscopic reaction pathways.

2. Materials and methods

2.1. Materials

Kaolinite KGa-1b (10.05 ± 0.02 m^2 /g surface area) was obtained from the Clay Mineral Society. Yttrium(III) chloride hexahydrate ($YCl_3 \cdot 6H_2O$, 99.9% purity) was purchased from Millipore Sigma (Burlington, USA). Indium internal standard (TraceCERT) and a REE mix standard (TraceCERT) were obtained from Sigma-Aldrich (St. Louis, USA). Potassium dihydrogen phosphate (KH_2PO_4, 99.0% purity), hydrochloric acid (HCl), and sodium hydroxide (NaOH) were purchased from Sigma-Aldrich. All solutions were prepared with ultrapure deionized water (18.2 MΩ·cm) produced by a Barnstead Nanopure system (Thermo Fisher Scientific, Waltham, USA).

2.2. Batch sorption experiment

Our recent study showed that Y and P exhibited distinct sorption behaviors on kaolinite across acidic to alkaline pH conditions (**Fig. S1**) and inferred that their interfacial interactions with kaolinite are strongly pH-dependent (Xu et al., 2025). To investigate this effect, four pH ranges were defined across pH 1–10 (**Fig. S1**). Since the competitive sorption mechanism at pH 6 was elucidated in our recent work (Xu et al., 2025), this study focuses on the rest of the pH regimes. Batch co-sorption and sequential sorption experiments were conducted to simulate Y—P interactions on kaolinite surfaces within these pH ranges. Detailed experimental parameters are provided in Table 1. Briefly, 1 g/L kaolinite suspensions were prepared following our previous procedure before batch experiments (Xu et al., 2025), sonicated for 1 h, and pre-equilibrated overnight on a magnetic stirrer at 5 Hz and room temperature.

2.2.1. Scenario I: co-sorption at pH 2

Because both Y and P displayed minimal surface sorption at pH 2 (**Fig. S1**), batch co-sorption experiments were performed by simultaneously adding 10, 20, and 50 mM Y and P to the prepared kaolinite suspensions, followed by 24 h reaction.

2.2.2. Scenario II: sequential sorption at pH 4

At pH 4, selective uptake was observed with maximum P and negligible Y sorption (**Fig. S1**). Sequential sorption experiments (4-500P-500Y) were therefore performed in two steps (each with 24 h reaction time) to ensure steady state. In Step 1 (P sorption): 500 μM P was spiked into the prepared kaolinite suspensions and allowed to react for 24 h. In Step 2 (Y sorption), the kaolinite solids after P pre-sorption were collected by centrifugation on the Eppendorf Centrifuge 5804 R at 10,000 rpm for 15 min and rinsed to remove residual aqueous phosphate following our previously established protocol (Xu et al., 2025). The rinsed pastes were resuspended in DI water before introducing 500 μM

Table 1
Experimental sets, corresponding annotations, sorption sequences of yttrium (Y) and phosphate (P) in sequential-sorption and control experiments. Note: Set I–VII are sequential sorption; Control IV– VII are corresponding controls. N/A: not applicable.

	Experimental sets	pH	Label	Addition sequences of species	
				Step 1 (24 h)	Step 2 (24 h)
Simultaneous sorption of Y and P					
Scenario I (Co-sorption)	Set I	2.0	2-10YP	10 mM Y and P	N/A
	Set II		2-20YP	20 mM Y and P	N/A
	Set III		2-50YP	50 mM Y and P	N/A
Sorption of P onto kaolinite, followed by Y					
Scenario II (Sequential sorption)	Set IV	4.0	4-500P-500Y	500 μM P	500 μM Y
	Control IV		4-500Y	N/A	500 μM Y
Sorption of Y onto kaolinite, followed by P					
Scenario III (Sequential sorption)	Set V	9.0	9-500Y-100P	500 μM Y	100 μM P
	Control V		9-100P	N/A	100 μM P
	Set VI		9-500Y-500P	500 μM Y	500 μM P
	Control VI		9-500P	N/A	500 μM P
	Set VII		9-500Y-1000P	500 μM Y	1000 μM P
	Control VII		9-1000P	N/A	1000 μM P

Y. A control experiment (4-500Y) was performed by 500 μM Y sorption onto kaolinite under identical conditions. At the start and end of each step, 2 mL of the aliquots were filtered via 0.22-μm Millipore membrane and analyzed for dissolved Y by inductively coupled plasma mass spectroscopy (ICP-MS, Agilent 7900a).

2.2.3. Scenario III: sequential sorption at pH 9

Y displayed the maximal sorption onto kaolinite, whereas P uptake was minimal at pH 9 (**Fig. S1**). Sequential experiments were thus performed in the reverse order at pH 4, with 500 μM Y first introduced into the suspensions and reacted for 24 h (Step 1, Y sorption). The solids were then rinsed by DI water, collected, and resuspended in DI water before 100 μM, 500 μM, and 1000 μM of P was added (Step 2, P sorption). Parallel phosphate-only sorption experiments were conducted with 100, 500, and 1000 μM P served as controls (9-100P, 9-500P, and 9-1000P). Initial and final aqueous samples (2 mL) were collected for phosphate measurement using the phosphomolybdate colorimetric assay on an ultraviolet-visible (UV − vis) spectrometer (Carey 60, Agilent) (Murphy and Riley, 1962).

Throughout the pre-equilibration and reaction, pH was maintained using 0.1 or 1 M HCl/NaOH. All sorption experiments were performed in triplicate. The reacted solids from all the batch experiments were collected by filtering through 0.22-μm membranes, freeze-dried, and stored at −80 °C for further characterization.

2.3. Analytic methods

2.3.1. Inductively coupled plasma mass spectrometry (ICP-MS)

REE standards (SPEX CertiPrep Inc.) and all solution samples were acidified with 2% HNO_3 (*v*/v) with 20 ppb of indium (In) as an internal standard before analysis by ICP-MS (Agilent 7900a). The mass spectrometer was optimized to maximize sensitivity, minimize isobaric interference ($CeO^+/Ce^+ < 1\%$) and doubly charged ions (<2%). The aqueous ^{89}Y concentrations were quantified, with calibration standards verified for every 20 samples to maintain accuracy.

2.3.2. Solid-state NMR spectroscopy

The coordination environments of phosphate species in reacted solids were characterized using ^{31}P direct polarization magic angle spinning (DP/MAS) NMR spectroscopy. The finely grind samples were loaded into a 4 mm diameter zirconia rotor and spun at 10 kHz. The 1D ^{31}P DP/MAS NMR spectra were collected on a Buker AVIII-HD 300 MHz two-channel NMR spectrometer (Rheinstetten, Germany) with an acquisition time of 24.6 ms and a repetition delay of 5 s. The 1024–2048 scans were conducted for each sample to achieve a reasonable signal to noise.

To characterize the surface atomic structures on kaolinite, the $^1H \rightarrow {}^{31}P/{}^{27}Al$ CP-REAPDOR solid-state NMR were conducted on a Bruker AVIII 400 three-channel NMR spectrometer (Rheinstetten, Germany) equipped with a MAS triple-resonance probe operating with a single coil tuned to ^{27}Al, ^{31}P, and ^1H. The ^{31}P 180° pulse length was set to 10 μs, while the ^{27}Al recoupling pulse applied midway through the dephasing sequence was adjusted to 1/5 of the rotor period with a radiofrequency field strength of 75 kHz. Two sets of echo trains were recorded in an interleaved manner: a dipolar dephasing spectrum (S) introducing ^{27}Al recoupling pulse and a second control sequence (S_0) without this pulse. Each spectrum was collected with 1024 scans, and eight independent runs of REAPDOR experiments were performed per sample over ~24 h. The difference spectrum (ΔS) was obtained by direct subtraction of the two datasets peak intensity ($\Delta S = S_0 - S$) at the same dephasing sequence length (τ). The normalized dephasing parameter was calculated by $\Delta S/S_0$. To analyze the dephasing effects, numerical simulation of $^1H \rightarrow {}^{31}P/{}^{27}Al$ CP-REAPDOR experiments were performed with SPINEVOLUTION program (Veshtort and Griffin, 2006; Xu et al., 2025). The pulse sequence and experimental settings were reproduced in the simulations, modeling a two-spin system (one ^{31}P and one ^{27} Al) with internuclear distances ranging from 2 to 6 Å.

2.3.3. Synchrotron X-ray absorption spectroscopy

The selected dried solids (**Table S1**) were evenly dispersed and dusted onto Kapton tape for synchrotron XAS analysis. Y K-edge extended X-ray absorption fine structure (EXAFS) spectra were collected at Beamline 6-BM of the National Synchrotron Light Source II (NSLS-II) at Brookhaven National Laboratory (Upton, NY, USA). A Si(111) double-crystal monochromator was used to control the incident beam energy. All Y K-edge EXFAS data were collected in fluorescence mode, with a Y_2O_3 foil (K-edge at 17038 eV) measured simultaneously for energy calibration. For each sample, 4–6 scans were collected and averaged.

The Y K-edge EXAFS spectra were calibrated, energy-aligned, and normalized using Athena (Ravel and Newville, 2005). The $\chi(k)$ functions were Fourier transformed using k^3 weighting, and the resulting spectra were fitted over a k range of 3−10.8 $Å^{-1}$ and an R range of 1.1−4 Å in Artemis (Ravel and Newville, 2005). Theoretical backscattering paths were generated with FEFF6 calculation using rhabdophane and xenotime as the structural model. The amplitude reduction factor (S_0^2) was fixed at 1.0 to reduce parameter covariance during fitting. This value produced reasonable first-shell coordination numbers, which was consistent to previous studies reported for clay-Y systems (Borst et al., 2020a). Single-scattering paths of Y–O, Y–P, Y–Y, and a multiple scattering Y–O, Y–P, were included in the fits. The coordination number (CN) and the interatomic distances were refined during fitting.

2.3.4. Electron microscopy

Surface morphology and elemental composition of reacted solids were examined using a scanning electron microscopy (SEM) (Hitachi SU8230, Tokyo, Japan). SEM images were acquired at a voltage of 10 kV and a current of 10 μA with a working distance of 8 mm. Energy-dispersive X-ray spectroscopy (EDS) analyses were performed at 20 kV and 30 μA with a working distance of 15 mm using an Oxford X-MaxN EDX detector. Transmission electron microscopy (TEM), high-resolution

TEM (HRTEM), and scanning transmission electron microscopy (STEM)-EDS were conducted on a Hitachi HD2700 (Tokyo, Japan) at 200–300 kV to further characterize the detailed surface structure, morphology, and elemental distribution. High-angle annular dark-field (HAADF) images were acquired in STEM mode to obtain *Z*-contrast. Imaging data were processed using Gatan software Rev. 3.5.3.4137 (Mitchell, 2008).

2.3.5. X-ray diffraction

X-ray diffraction (XRD) analysis was performed to characterize the mineralogical composition of kaolinite before and after sorption experiments. Finely ground samples were analyzed using a Rigaku Miniflex Powder XRD (Tokyo, Japan) equipped with a Cu Kα radiation source ($\lambda = 1.5406$ Å) at 30 kV and 10 mA. Diffraction patterns were collected over a 2θ range of 5°–90° with a step size of 0.02° and a scan speed of 1° per minute. The data was analyzed using Jade software for phase identification of the newly formed REE-containing solids formed under different pH conditions (Bellifemine et al., 2001).

3. Results

3.1. Uptake of aqueous Y and P by kaolinite

In Scenario I (pH 2.0), sorption of both Y and P was negligible (**Fig. S1**), which suggests that Y—P interaction occurred primarily in aqueous phase. To simulate this scenario, 10–50 mM Y and P were simultaneously added to kaolinite suspensions. The resulting solid phases were characterized by SEM and XRD, and the structural information is provided in **Section 3.2**.

In Scenario II (pH 4.0), Y sorption remained minimal, whereas P achieved maximum uptake onto kaolinite (**Fig. S1**). A sequential sorption experiment was therefore designed to simulate secondary chemical weathering, in which P released from mineral dissolution or decomposition of biogenic input preferentially binds to kaolinite, followed by interaction with dissolved Y (Ruttenberg and Berner, 1993). Y uptake in the sequential sorption experiment (4-500P-500Y) reached 42.64%, whereas negligible uptake was observed in the control without P pre-sorption (4-500Y) (Fig. 1a). The results indicate that the pre-sorbed P facilitates Y retention, and thus aqueous Y interacts primarily with surface-bound P rather than directly with kaolinite surface.

However, Scenario III (pH 9) displayed the opposite pattern: sorption of Y reached the maximum, while minimal P sorption was observed (**Fig. S1**). Sequential sorption was therefore conducted in reverse order. To evaluate the effect of P concentrations as a ligand, three sets with 100, 500, and 1000 μM P in Step 2 (9-500Y-100P, 9-500Y-500P, 9-500Y-1000P, Sets V–VII) were performed, which showed similar trends (Fig. 1b). Specifically, P uptake was 95.34%, 44.64%, and 50.64%, respectively, whereas controls without prior Y sorption (Control V–VII) showed nearly no uptake (Fig. 1b). The lower P uptake% at a higher P concentration can be attributed to the saturation of sorption sites on kaolinite surface. These findings indicate that, although direct P sorption onto kaolinite is unfavorable under alkaline conditions, pre-sorbed Y on kaolinite surface promotes P sorption. Further characterizations were conducted to examine the surface products arising from these Y—P interactions. To better quantify the sorption capacity, we converted the uptake percentages into mass-normalized solid-phase concentrations (**Table S2**). Overall, the normalized data followed trends similar to the uptake results. Notably, although 9-500Y-1000P group showed a lower uptake percentage than the 9-500Y-500P treatment, its mass-normalized P loading was higher due to higher initial P concentrations, which resulted in a more reasonable trend in solid-phase P accumulation and indicate enhanced Y—P interactions during sorption at elevated P concentrations.

The distinct uptake behaviors of Y between the sequential sorption groups vs. the control groups demonstrate that i) pH strongly influences Y sorption behaviors and mobility on kaolinite surface in the presence of phosphate, and ii) pre-sorbed species (i.e., P under weak acidic and Y

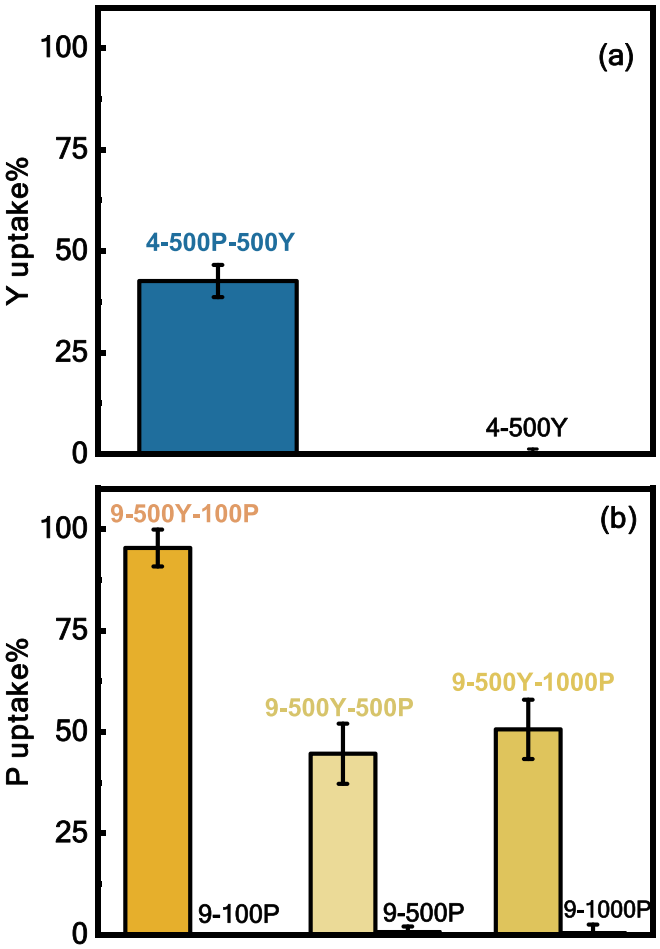

Fig. 1. (a) Yttrium uptake of sequential-sorption experiments and the corresponding control at pH 4, and **(b)** phosphate uptake of sequential sorption experiments and control at pH 9. Blue and yellow bars denote the sequential sorption sets. Note: sequential sorption at pH 4 was performed by first introducing P, followed by adding Y; the addition sequences at pH 9 were inversed; Controls consist of single solute additions: Y-only at pH 4 and P-only at 9. (For interpretation of the references to colour in this figure legend, the reader is referred to the web version of this article.)

under alkaline conditions) interact with aqueous species and lead to increased uptake. The interfacial mechanisms responsible for these pH-dependent interactions were examined through solid-phase characterization in the following sections.

3.2. Solid-phase characterization of reacted products from Scenario I (pH 2)

3.2.1. P speciation characterization by 1D ^{31}P NMR

Direct-polarization MAS ^{31}P solid-state NMR was employed to characterize phosphate species at kaolinite surfaces, which enables qualitative assessment of inner−/outer- sphere complexes, surface ternary complexes, and surface precipitates from their characteristic chemical shifts (δ_p) (Li et al., 2013; Xu et al., 2025). One-dimension ^{31}P NMR spectra were collected for 10 mM Y—P cosorption (2-10YP) and compared with a reference coprecipitate prepared under identical solution conditions but in the absence of kaolinite (**Text S1**). Both spectra displayed two well-defined resonances centered at chemical shifts of –1.2 ppm and –10.7 ppm, indicating the phosphate nuclei occupied similar coordination environments in both system (**Fig. S2**). Gaussian deconvolution resolved the spectra into two components with comparable integrated areas with an overall fitting goodness of 0.95. These

results provide strong evidence that the Y—P precipitate formed during co-sorption at pH 2.

3.2.2. Morphology and mineralogy characterization by SEM-EDS and XRD

SEM-EDS revealed that the morphology of Y—P coprecipitates gradually evolved as the Y and P concentrations increased. The coprecipitates appeared as irregularly shaped aggregates grown on kaolinite surfaces at 10 mM and 20 mM (**Fig. S3a and b**) and transformed into acicular (needle-like) crystallites at 50 mM (**Fig. S3c**). A similar needle-like morphology was also observed in Y—P coprecipitates without kaolinite (**Fig. S4**, **Text S1**). XRD analysis further confirmed a concomitant evolution in crystallinity with rising co-sorption concentrations. At 10 mM, the diffraction pattern of Y—P coprecipitates was not notably different from that of the pristine kaolinite, even though the coprecipitates were visually observed by SEM (**Fig. S5a**). At 20 mM, broad humps were observed, indicating the predominance of newly formed amorphous phase (**Fig. S5a**). When the concentration was increased to 50 mM, additional sharp diffraction peaks appeared, which belong to churchite (**Fig. S5b**). These XRD results clearly demonstrated the transition from amorphous to well-crystallized Y—P coprecipitates as solute concentrations increased.

3.3. Solid-phase characterization of reacted products from Scenario II (pH 4) and III (pH 9)

3.3.1. P speciation characterization by 1D ^{31}P NMR

^{31}P DP/MAS solid-state NMR spectra were acquired for samples from pH 4 and 9. For Scenario II at pH 4, two references were analyzed alongside the sequential sorption sample: i) 500 μM phosphate-only sorption (4-500P) and ii) 10 mM Y—P coprecipitate (**Text S1**). The 4-500P spectrum showed a single resonance at ~−10 ppm (Fig. 2a), consistent with phosphate bound in an aluminophosphate inner-sphere complex, as previously reported for Al-coordinated phosphate (−5 to −35 ppm), where Al shielding shifts the signal upfield (Lookman et al., 1994; Poulsen et al., 2010). By contrast, the sequential sorption sample (4-500P-500Y) exhibited an asymmetric spectrum with two prominent peaks at δ_p= −1.91 ppm and −10.85 ppm, and a shoulder at δ_p= −4.33 ppm (Fig. 2a **and S6b**). This line shape resembles that of the bulk of 10 mM Y and P coprecipitate, which showed resonances at 1.53, −1.91, −4.33, and −9.92 ppm (Fig. 2a **and S6a**). Gaussian deconvolution reproduced all spectra reasonably (R^2 = 0.95–0.99), with only minor variations in the chemical shift and linewidth (Fig. 2a **and S6; Table S3**). The recurring signals at approximately −1.91, −4.33, and −10 ppm in both the sequential sorption and coprecipitation samples suggest the formation of Y—P precipitates or related Y-P-kaolinite complexes during sequential sorption. These interfacial species likely accounted for the enhanced Y uptake discussed in Section 3.1, by partitioning Y from aqueous phase onto kaolinite surfaces. Additional characterization is required to confirm this possibility.

For Scenario III (pH 9), the samples 9-500Y-500P and 9-500Y-1000P were analyzed. Both spectra were dominated by three distinct peaks at 1.77, −3, and −10 ppm (Fig. 3b **and S7**). Comparison with a bulk Y—P coprecipitate reference, which showed resonances at 1.77, 1.77, −4.2, and −10 ppm (**Text S1 and Fig. S7**), revealed close alignment except for a deviation at −3 ppm. Peak deconvolution resolved −3 ppm envelope into two components centered at −1.77 and −4.2 ppm with R^2 = 0.99

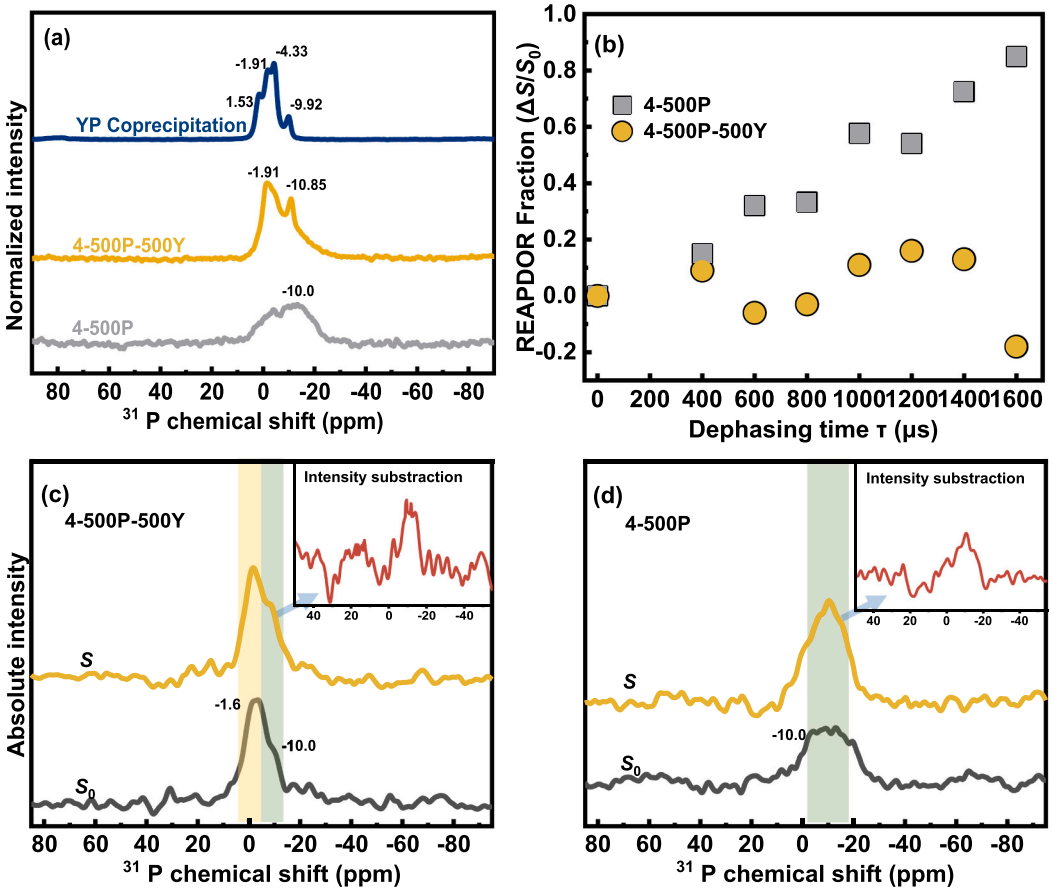

Fig. 2. (a) 1D ^{31}P solid-state NMR spectra for sequential-sorption experiments (4-500P-500Y), control (4-500P, phosphate sorption only), and reference (10 mM Y—P coprecipitation) at pH 4; **(b)** ^{31}P/^{27}Al REAPDOR fraction curve for 4-500P-500Y and 4-500P; **(c)** and **(d)** REAPDOR NMR spectra for dipolar dephasing spectrum (*S*) and control spectrum (S_0). Green and orange vertical shadings represent the chemical shift approximately at −1.6 ppm and −10 ppm, respectively. (For interpretation of the references to colour in this figure legend, the reader is referred to the web version of this article.)

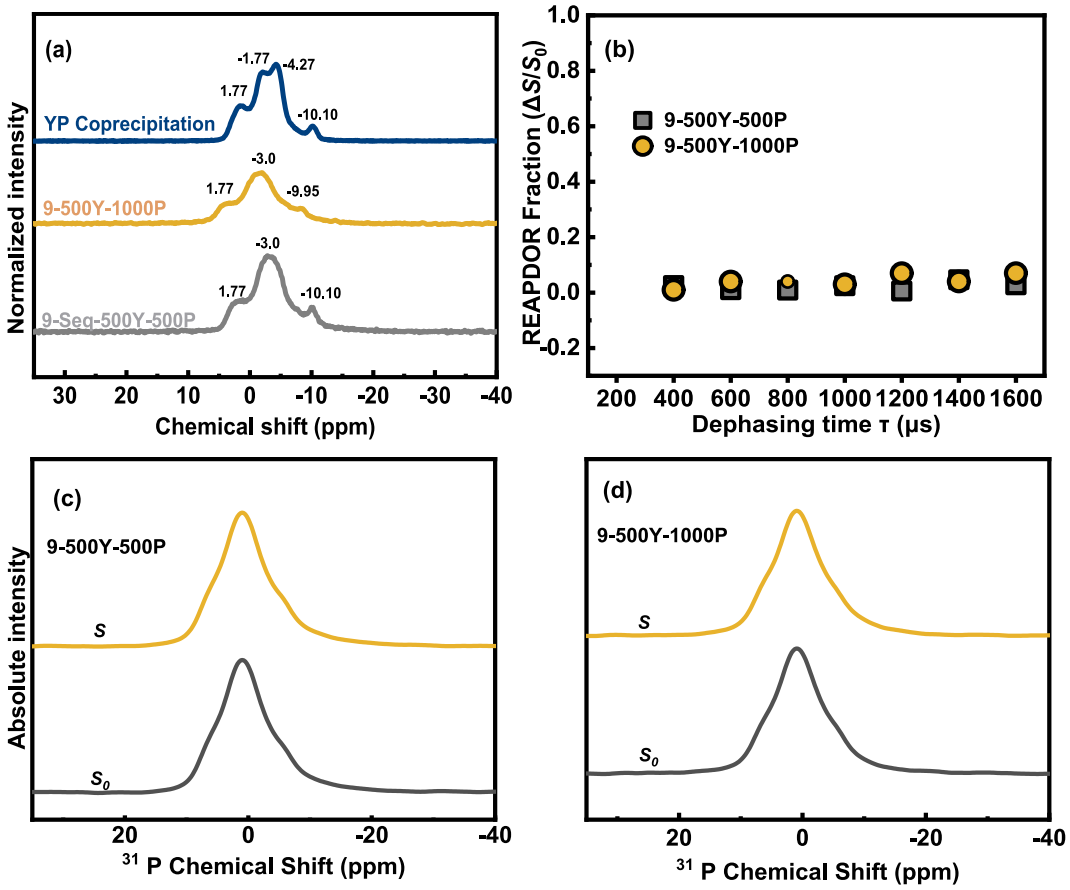

Fig. 3. **(a)** 1D ^{31}P solid-state NMR spectra for sequential-sorption experiments (9-500Y-500P and 9-500Y-1000P), and reference (10 mM Y—P coprecipitation) at pH 9; **(b)** ^{31}P/^{27}Al REAPDOR fraction curve for 9-500Y-500P and 9-500Y-1000P; **(c)** and **(d)** REAPDOR NMR spectra for dipolar dephasing spectrum (S) and control spectrum (S_0).

(**Fig. S7 and Table S3**), which indicates broadly comparable phosphate coordination environments in sequential sorption samples and bulk coprecipitates. Such small chemical-shift deviations may reflect the alterations of the relative abundance of P species, structural disorder, or minor distortions in Y—P surface complexes compared to the bulk coprecipitated phases (Mathew et al., 2011). A plausible explanation is that sequential sorption samples exhibited greater structural heterogeneity as the interactions with pre-sorbed Y at water-mineral interfaces creating multiple coordination environments. This interpretation aligns with previous studies in which phosphate bound in heterogeneous environments exhibit broadened and slightly shifted ^{31}P signals due to varying surface interactions and local binding geometries (Hunger et al., 2004).

3.3.2. *Characterization of P local bonding by $^{1}H \rightarrow {}^{31}P/{}^{27}Al$ CP-REAPDOR*

In our previous study, ^{1}H → ^{31}P/^{27}Al CP-REAPDOR was applied to probe interfacial structure after sequential sorption at pH 6 (Xu et al., 2025). This method targets phosphate nuclei in close proximity to Y and distinguishes Y—P associations occurring on the Al-octahedral layers of kaolinite. Building on this approach, we employed the ^{1}H → ^{31}P DP/MAS REAPDOR experiments with ^{27}Al dephasing to characterize phosphate coordination environments neighboring aluminum. The heteronuclear ^{31}P−^{27}Al dipolar couplings extracted from the spectra provide crucial distance information between phosphate and the kaolinite surfaces (Li et al., 2013). Two sets of spectra S and S_0 were collected with and without ^{27}Al dephasing, respectively. The REAPDOR fraction ($\Delta S/S_0$) were obtained as a function of dephasing time, where a lower fraction indicates longer ^{31}P−^{27}Al distance. It is noted that the dephasing effect of REAPDOR is sensitive to ^{31}P- ^{27}Al distance ≤6 Å, and any longer distances would not be captured based on REAPDOR fraction curve.

In Scenario II (pH 4), the sequential sorption sample (4-500P-500Y) showed a REAPDOR fraction essentially around zero throughout the dephasing period (Fig. 2b), indicating no detectable ^{31}P−^{27}Al dipolar interaction. This suggests that most phosphate nuclei were located more than ~6 Å from the kaolinite surface. The phosphate-only sorption control (4-500P), in contrast, exhibited a steadily increasing REAPDOR fraction reaching ~0.85 at the longest dephasing time (Fig. 2b), consistent with phosphate rigidly coordinated to surface Al. Detailed analysis for the ^{31}P/^{27}Al DP REAPDOR NMR spectra further corroborated this interpretation: the 4-500P spectrum showed a major peak at −10 ppm and a significant signal loss from S_0 (without ^{27}Al dephasing) to S (with ^{27}Al dephasing) (Fig. 2d). A synthetic $AlPO_4$ reference produced a similar fraction curve and dephasing behaviors (**Fig. S8**). SPINEVOLUTION simulations indicated that this rigid structure corresponded to a monodentate P−O− Al binding with a P−Al distance of ~3.6 Å (**Fig. S9**). By contrast, the REAPDOR spectra of 4-500P-500Y displayed an asymmetrical shape with peaks of −1.6 ppm and −10 ppm (Fig. 2c), matching the assignments in the 1D ^{31}P NMR data (**Fig. S6 and Table S3**). Only small portion of peak at −10 ppm underwent signal loss and dephasing, attributable to an inner-sphere complex with Al-octahedral layers. The dominant peak at −1.6 ppm, assigned to phosphate nuclei in Y—P precipitates, remained non-dephasing, confirming a ^{31}P−^{27}Al distance greater than 6 A°.

The spectral characterization at pH 9 was broadly similar to pH 4. The sequential sorption samples (9-500Y-500P and 9-500Y-1000P) maintained REAPDOR fraction ~0 over the full dephasing period

(Fig. 3b), which indicate the absence of Al-proximal phosphate. The fraction curve was more stabilized and flatter than those at pH 4, reflecting the lack of even minor Al-bound phosphate contributions. This is best visible by comparing individual spectra S and S_0 for a single dephasing delay (Fig. 3c and d). Detection of near identical spectra further validates the absence of detectable Al-proximal phosphate. Together with the increased phosphate uptake observed only after Y pre-sorption (Fig. 1), under conditions where phosphate sorption onto kaolinite was otherwise unfavorable, these results strongly support the formation of Y—P precipitates on kaolinite surface, thereby eliminating measurable $^{31}P-^{27}Al$ dipolar coupling.

3.3.3. Morphology characterization by TEM-EDS

To further examine the morphology and distribution of Y—P precipitates, TEM characterization was performed on the solid products collected from the three sequential sorption treatments, 4-500P-500Y at pH 4, and 9-500Y-100P and 9-500Y-1000P at pH 9. All samples displayed newly formed, aggregated particles with irregular shapes (Fig. 4), which exhibited morphologies distinct from the clean surfaces and edges of pristine kaolinite particles (**Fig. S10**). High-resolution TEM images of precipitates attached at kaolinite edges showed subtle or no clearly resolved lattice structures, in contrast with the well-defined kaolinite lattice. Fast Fourier Transform (FFT) analysis of precipitates showed diffuse diffraction rings with weak and broadened reflection features rather than sharp diffraction spots or highly resolved rings, indicating limited long-range structural ordering within solids and the presence of amorphous to polycrystalline phases (**Fig. S11**). STEM-EDS was then used to examine the chemical composition and distribution of these aggregates. The high-angle annular dark-field (HAADF) images revealed regions of elevated Z-contrast distributed on kaolinite surfaces, which indicates enrichment in elements that are heavier than those in kaolinite (**Fig. S12a, S13a, and S14a**). The corresponding EDS spectrum confirmed that these high-contrast regions contained Y and P, and the elemental maps showed strong overlap between Y and P distribution (**Fig. S12d, 13d, and 14d**). Collectively, these observations provided compelling evidence for the formation of Y—P surface precipitates. Nevertheless, the weak-to-no crystallinity of precipitates make definitive mineralogical identification challenging, and further analysis of Y local bonding environments was therefore necessary.

3.3.4. Characterization of Y local bonding by XAFS

XAFS spectroscopy was employed to further characterize Y local bonding environments. Two sequential sorption samples prepared at pH 4 and 9 were selected as representatives, with corresponding co-sorption

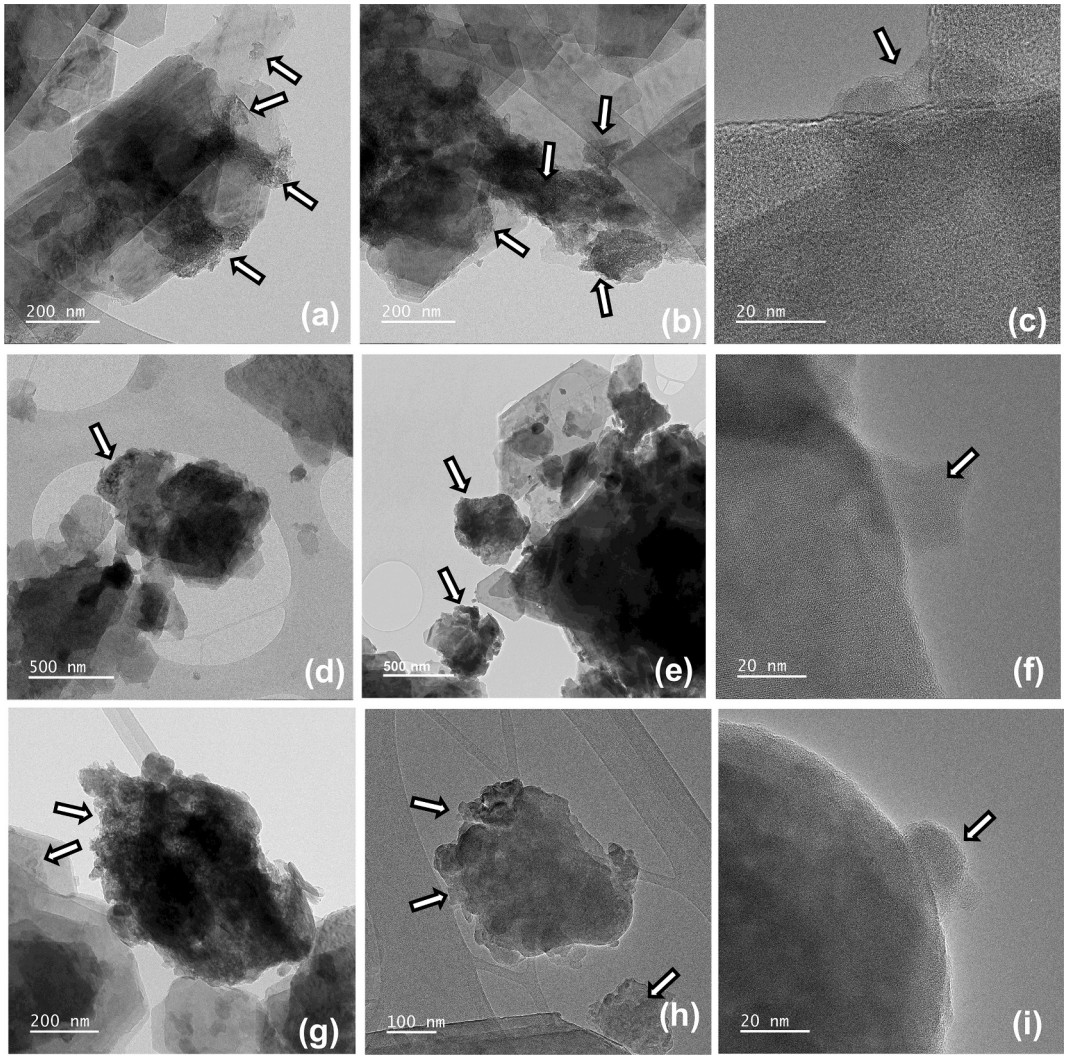

Fig. 4. TEM images of sequential-sorption samples. **(a)—(b)** images of sample 4-500P-500Y with 500 μM yttrium sorption followed by 500 μM phosphate at pH 4, and **(c)** corresponding HRTEM image. **(d)—(e)** images of sample 9-500Y-100P with 500 μM yttrium sorption followed by 100 μM phosphate at pH 9, and **(f)** HRTEM image of the same specimen. **(g)—(h)** images of 9-500Y-1000P with 500 μM yttrium sorbed first followed by 1 mM phosphate at pH 9, and **(i)** corresponding HRTEM image. White arrows indicate the newly formed surface precipitates.

samples synthesized under identical conditions used for comparison (**Text S1 and Table S1**). Additionally, a Y sorption-only sample at pH 9 and a xenotime crystal (YPO_4) were analyzed for additional comparison. All Y K-edge X-ray absorption near edge structure (XANES) spectra exhibited a main peak at ~17,062 eV (Fig. 5). A weak shoulder feature at ~17,073 eV was observed only in the sequential- and co-sorption samples, but not in the Y-sorption only spectrum. Previous studies have shown that Y K-edge XANES spectra of phosphate-associated phases typically display a characteristic "strong peak-weak shoulder" feature that is apparently different from other Y-phases (e.g., carbonate- or organics-associated phases) (Liu et al., 2020). Such a spectral feature can be attributed to: (i) Y occupying higher point-symmetry sites, which was found more pronounced absorption features, especially a double or triple-peaks (Borst et al., 2020b); and (ii) phosphate coordination may modify the local symmetry and electronic structure around Y, giving rise to distinct final-state features in the XANES spectrum (Miessler et al., 2014).

EXAFS analysis provided further insight into Y local coordination. The Fourier transform (FT) spectra revealed a dominant first-shell feature at ~1.8 Å and a weaker second-shell feature at ~2.8 Å (both uncorrected for phase shift) (Fig. 6b). The first shell was well fitted with a Y- O path, using a fixed S_0^2, which gives uniform Y- O distance of 2.34–2.36 Å and first-shell CN ranging from ~8.0–9.0, with fixed CN values indicated by asterisks (Table 2). These values agree with the reported first-shell Y- O bond lengths in Y-bearing references such as YPO_4,Y_2O_3, and hydrated Y ion in aqueous solution (Borst et al., 2020a). Fitting the second shell was more complex. Both Y- P and Y- Y paths were incorporated, and the results at both pH 4 and 9, were broadly consistent with rhabdophane (hydrated $REEPO_4$) as a structural model. The refined CNs were ~ 0.6–1.7 for Y-P and ~ 0.9–1.8 for Y-Y paths (Table 2). Interestingly, the Debye-Waller factor (σ^2), which reflects structural disorder, showed a pH dependence. For sequential- and co-sorption samples at pH 9, σ^2 values were relatively stable (Table 2). In contrast, fitting the pH 4 samples were more challenging. When CN and σ^2 were released for all paths, the models produced unreasonable values. Therefore, the first-shell CN and σ^2 value of Y—Y path were fixed for the sequential sample at pH 4 to stabilize the fit. This requirement for additional fixed parameters suggests that Y–P associated phases formed under weakly acidic conditions are structurally more disordered than those formed under alkaline conditions. One possible explanation is that at pH 4, phosphate sorption was less extensive than the initial Y sorption at pH 9, which reduced the availability of surface sites for subsequent interfacial reactions, and consequently limited the formation of surface precipitates.

Comparison with xenotime crystal reference also highlights the dependence of σ^2 on crystallinity. In xenotime, Y is coordinated by two distinct P shells: Y–P1 at ~3.0 Å and Y–P2 at ~4.0 Å (Table 2). In our sorption samples, however, only the Y–P1 path could be reasonably fitted, whereas incorporation of the Y-P2 path consistently yielded unrealistically high σ^2 value (**Table S4**). Attempts to constrain the CNs to xenotime values resulted in increased σ^2 for the Y- P2 path (**Table S4**). These results provided further evidence of distorted Y—P bonding environments and greater structural disorder in the sorption samples, implying the formation of polycrystalline or amorphous phases in

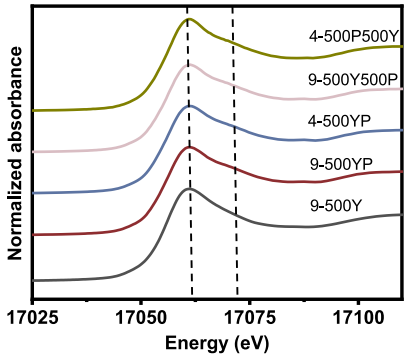

Fig. 5. Y K-edge XANES spectra of Y—P sequential sorption (4-500P-500Y, 9-500Y-500P), Y—P co-sorption (4-500YP, 9-500YP), and Y sorption-only (9-500Y) samples at pH 4 and 9.

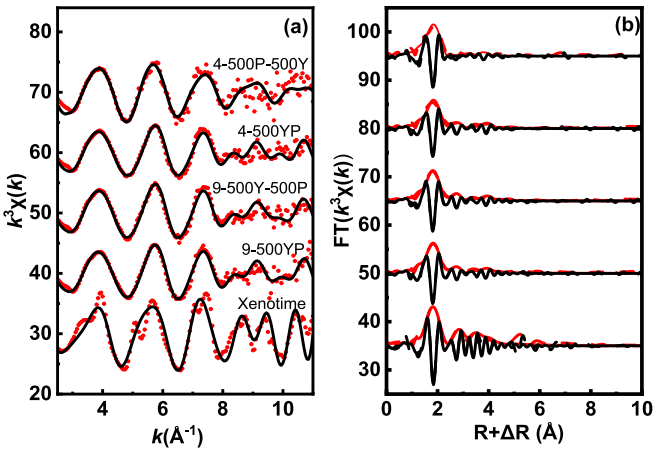

Fig. 6. **(a)** The k^3-weight EXAFS data (red dots) with best fit (black solid lines); **(b)** corresponding Fourier transform magnitudes and imaginary components (red and black dashed lines, respectively) and best fit in *R*-space (red and black solid lines). (For interpretation of the references to colour in this figure legend, the reader is referred to the web version of this article.)

Table 2
Y K-edge EXAFS fitting parameters for sequential sorption, co-sorption samples, and xenotime crystal at pH 4 and pH 9.

Sample	Path	CN[a]	R (Å)[b]	σ^2 (Å^2)[c]	ΔE_0 (eV)[d]	S_0^2 [e]	R-factor [f]
4-500P-500Y	Y-O	8*	2.36 (3)	0.008	0.05 (4)	1.0*	0.032
	Y-P1	0.63 (0)	3.06 (7)	0.002			
	Y-Y	1.1(5)	4.19 (6)	0.005*			
4-500YP	Y-O	8.9 ± 1.5	2.36 (0)	0.01	0.31(6)	1.0*	0.025
	Y-P1	1.7 (2)	3.08 (7)	0.007			
	Y-Y	1.2 (0)	4.26 (6)	0.004			
9-500Y-500P	Y-O	8.5 ± 1.1	2.35 (7)	0.01	0.36(9)	1.0*	0.013
	Y-P1	1.2(2)	3.08 (3)	0.003			
	Y-Y	1.8(1)	4.26 (5)	0.007			
9-500YP	Y-O	8.2 ± 1.0	2.36 (0)	0.009	0.36(9)	1.0*	0.012
	Y-P1	1.6(0)	3.08 (6)	0.006			
	Y-Y	0.9(5) 93	4.25 (3)	0.002			
xenotime	Y-O	8*	2.34 (7)	0.005	5.47(7)	1.0*	0.019
	Y-P1	2*	3.03 (7)	0.002			
	Y-P2	4*	4.05 (8)	0.009			
	Y-Y	4*	3.66 (9)	0.01			
	Y-O-P2	8*	3.72 (1)	0.005			

Note: *fixed, [a] coordination number, [b] interatomic distance, [c] Debye-Waller factor, [d] energy shift, [e] amplitude factor, [f] fitting goodness.

contrast to the well-organized Y– P coordination in xenotime.

4. Discussion

4.1. pH effects on Y sorption behavior

These results underscore the key role of pH in controlling REE mobility, transport, and redistribution during chemical weathering. First, pH dictates the aqueous speciation of REE and natural ligands. Using Y and P as representative system, PRHEEQC calculation shows that protonated P species and free Y^{3+} are the major species under highly acidic conditions (**Fig. S15**). In the near-neutral region, Y—P aqueous complexes gradually become more dominant, which then start to precipitate as YPO_4 as pH further increases (**Fig. S15**). We can thus conclude that the acidic-to-neutral conditions facilitate Y transport and mobilization, whereas alkaline conditions favor precipitation and lead to immobilization. Second, these changes in speciation are also associated with pH-induced changes in mineral surface properties (especially surface variable charge), which together govern REE sorption behavior. Clay minerals are the principal substrates that interact with and retain REE during various weathering processes. Y sorption onto kaolinite increases steadily as pH rises (**Fig. S1**). On the other hand, maximum sorption of phosphate is achieved at pH 4−4.5 due to the strong electrostatic attraction between the dominant $H_2PO_4^-$ and the kaolinite surface (**Fig. S1**). Sorption of P declines at lower pH, owing to the dominant presence of uncharged H_3PO_4, and declines again at higher pH as the kaolinite surface charge becomes more negative (**Fig. S1**) (Xu et al., 2025). In addition, the saturation indices (SI) predicted by Visual MINTEQ indicated that precipitation of Y and P is thermodynamically more favorable under alkaline conditions (**Table S5**). Overall, the distinct sorption behaviors of Y and P strongly affect the dominant interfacial reaction pathways and govern solid-to-solution fractionation. The interfacial reaction pathways are driven by solution pH, which leads to pH-specific trends of REE occurrences and influences both the rate and extent of REE mineral weathering in the natural environments.

4.2. Proposed reaction mechanism

Our study elucidates the pH effects on REE behavior in the presence of phosphate during secondary chemical weathering and proposes potential reaction mechanisms in both the comparatively underexplored sedimentary deposits in the southeastern United States and classic IADs. Based on our results, the water-mineral interfacial reaction mechanisms can be grouped into four pH regimes (Fig. 7): i) extremely acidic, ii) acidic, iii) neutral, and iv) alkaline conditions. Under extremely acidic conditions, the minimum sorption of Y and P favors bulk coprecipitation (**Fig. S1 and** Fig. 7a). The crystallinity of these coprecipitates increases with solute concentrations, as higher Y and P levels more readily overcome the nucleation barrier, while lower concentrations yield amorphous phases. In natural settings over long time scales, sorption on mineral and surface complexation at low solute concentrations cannot be excluded and may act as a precursor to REE-phosphate precipitates or more crystalline REE-bearing minerals. As pH rises slightly into weak-acidic range, selective sorption becomes dominant (Fig. 7b). Kaolinite shows a higher affinity for phosphate (**Fig. S1**), and $^{1}H \rightarrow {}^{31}P/{}^{27}Al$ CP-REAPDOR combined with numerical modeling suggests that P forms monodentate inner-sphere complex with surface Al (~3.6 Å distance), which has not been previously reported. The pre-sorbed P subsequently reacts with dissolved Y to form surface precipitates. Surface complexation is likely the first step (eq. 1). Precipitation occurs when the concentrations are high enough to overcome the nucleation barrier (eq. 2).

$$\equiv Al-OH + H_2PO_4^- \rightarrow \equiv Al-O-HPO_3^- + H_2O \quad (1)$$

$$\equiv Al-O-HPO_3^- + Y^{3+} + nH_2O \rightarrow \equiv Al-OH + YPO_4 \bullet (n-1)H_2O_{(s)} + 2H^+ \quad (2)$$

Furthermore, in the near-neutral range (~pH 6), Y and P compete for

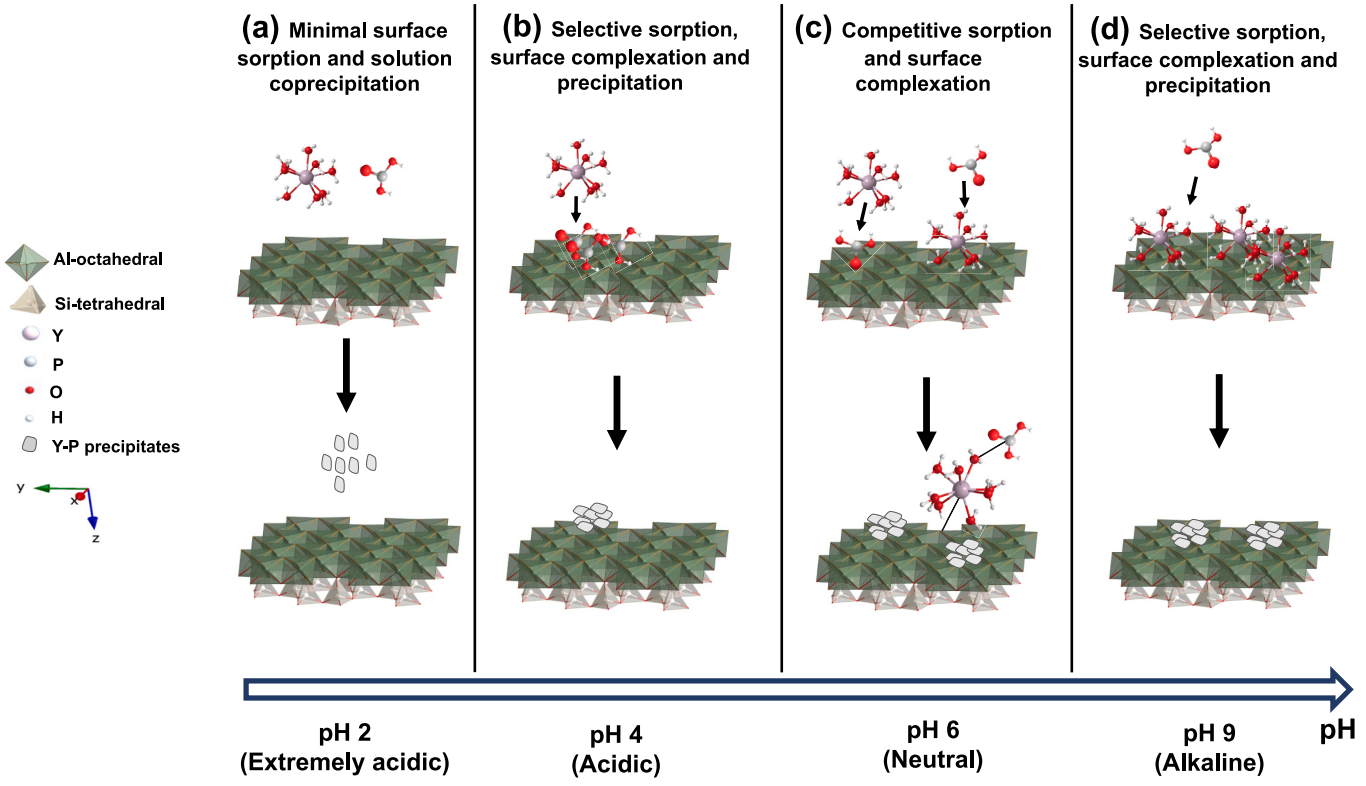

Fig. 7. Schematic of the proposed reaction mechanisms across the full pH spectrum: **(a)** highly acidic (pH 2); **(b)** weak acidic (pH 4); **(c)** neutral (pH 6); and **(d)** alkaline condition (pH 9).

adsorption sites on kaolinite surface and display comparable uptake (Fig. 7c) (Xu et al., 2025). By using $^{1}H \rightarrow {}^{31}P/{}^{27}Al$ CP-REAPDOR, we found that both kaolinite-Y-P surface ternary complexes (with ~5.5 Å P–Al distance) and Y—P surface precipitates are formed during sequential sorption, and the proportion of these two phases depends on the sorption sequence.

Finally, under alkaline conditions (Fig. 7d), Y is selectively sorbed on kaolinite while P sorption is negligible. The underlying mechanism of REE sorption on clay minerals remains controversial. Borst et al., revealed that Y and Nd formed 8- to 9- coordinated hydrated outer-sphere complexes using X-ray absorption spectroscopy (Borst et al., 2020a). Other studies reported a mixture of inner- and outer- sphere complex of REE on clay mineral surfaces (Eqs. 3–4). We integrate our results with both possibilities and propose that the pre-sorbed Y interacts with aqueous phosphate to enable surface precipitation (eqs. 5–6). Because alkaline solutions thermodynamically favor Y—P coprecipitations, this surface precipitation proceeds more readily than under other pH regimes (**Table S5**). It explains the more Y—P precipitates observed by TEM; and the longest P–Al distances inferred from the NMR REAPDOR fraction curve.

$$\equiv Al-OH + Y(OH)^{2+} \rightarrow \equiv Al-OH\cdots Y(OH)^{2+}_{(Outer-sphere)} \quad (3)$$

$$\equiv Al-OH + Y(OH)^{2+} + OH^{-} \rightarrow \equiv Al-O-Y(OH)^{+}_{(Inner-sphere)} + H_2O \quad (4)$$

$$\equiv Al-O-Y(OH)^{+}_{(Inner-sphere)} + HPO_4^{2-} + nH_2O \rightarrow \equiv Al-OH + YPO_4 \bullet nH_2O + OH^{-} \quad (5)$$

$$\equiv Al-OH\cdots Y(OH)^{2+}_{(Outer-sphere)} + HPO_4^{2-} + (n-1)\,H_2O \rightarrow \equiv Al-OH + YPO_4 \bullet nH_2O \quad (6)$$

It should be noted that the effects of P likely vary depending on the characteristics of geological settings. The effects may be more profound in P-rich environments, such as the sedimentary deposits discussed herein, while potentially playing a relatively minor role in classic IADs. Nevertheless, overall, P-associated interactions still represent an additional mechanistic pathway contributing to non-exchangeable REE pools alongside the extensively reported ion-exchangeable REE occurrences. Additionally, pH 4–6.5 is a common range observed in clay-rich REE deposits (Pan et al., 2024). Nevertheless, this study investigates the full pH spectrum and corresponding reaction mechanisms, aiming to use endmember conditions to systematically define and improve the understanding of REE behaviors under pH fluctuations and transient gradients during weathering. In addition, strongly acidic conditions may occur in certain geological settings, such as mining drainage systems, localized microenvironments with high microbial activity, and soils with extensive organic matters degradation (He et al., 2024; Lozano et al., 2020; Middleton et al., 2024; Ribeiro et al., 2020; Wu et al., 2025). Shifts toward circumneutral and alkaline conditions are also possible, especially in systems with elevated ionic strengths or carbonate-rich environments (Johannesson et al., 1996; Russo et al., 2025; Wood, 1990). Overall, natural REE reservoirs are highly complex systems, and future studies should consider additional environmental factors to build a broader and more comprehensive understanding of REE behaviors.

4.3. Implication for understanding the interfacial reactions during chemical weathering

This study reveals the critical role of pH in controlling REE surface sorption and relevant interactions with P, which is essential for understanding REE dissolution, transport, and redistribution during weathering processes. By examining the sorption behaviors of Y and P across the full pH spectrum, our results provide molecular-scale evidence for the underlying water-mineral interfacial reactions, establish a mechanistic basis for interpreting field observations, and link sorption experiments under controlled conditions to real interactions in complex natural settings. In highly weathered REE deposits, pH commonly varies across vertical profiles. Field investigations have demonstrated that soil-solution pH is an important factor controlling the vertical distribution of exchangeable REE. For instance, in a crust elution-deposits in Guangxi Province, China, pH increases from ~4.0 at the surface to ~6.5 at depth, coinciding with marked enrichment of exchangeable REE in the deeper horizons (Pan et al., 2024).

In addition to the terrestrial environments, pH also significantly influences REE behavior in aquatic systems. For example, rainwater equilibrated with atmospheric CO_2 typically retains pH to ~5.7. This mildly acidic condition favors REE transport by stabilizing REE-carbonate complexes. By contrast, increasing pH promotes REE retention through precipitation as REE hydroxides or carbonates, exchange of REE for H^+ on accessible mineral sites, as well as enhanced adsorption (Elderfield, 1988; Stumm and Morgan, 2013). Similarly, case studies of REE transport in coastal aquifers have revealed strong correlations between pH and REE sorption-desorption dynamics, as well as fractionation in organic and inorganic complexes (Amiel et al., 2024). Our findings contribute to addressing the knowledge gap between these field observations and the underlying reactions operating at water-mineral interface. This study highlights the importance of enriching the geochemical toolbox available for predicting REE behaviors in natural environments, which potentially inform REE identification and prediction in complex geological settings. A thorough understanding of key geochemical constraints on the underlying reaction mechanisms at the water-mineral boundary is necessary to trace the REE transport and distribution, and to identify REE resources.

5. Conclusion

This study investigated the pH-dependent Y sorption on kaolinite in the presence of phosphate. The interfacial reaction mechanisms involved in the sequential sorption of Y and P were proposed and substantiated by a complementary suite of advanced analytical techniques including NMR and synchrotron XAS. Under strongly acidic conditions (pH ~2), Y and P coprecipitated in the bulk solution, and the crystallinity of the precipitate increases at higher initial concentrations of Y and P. At mildly acidic conditions (pH 4), P was preferentially sorbed onto kaolinite, which then complexed with aqueous Y and coprecipitated on the kaolinite surface. In the near neutral range (pH ~6), competitive sorption of Y and P yielded ternary surface complexes (kaolinite-Y-P), as revealed by a ^{31}P– ^{27}Al distance of ~5.5 Å. Under alkaline conditions, Y sorption became dominant, and Y precipitated with dissolved P on kaolinite surface via interfacial interactions.

CRediT authorship contribution statement

Hang Xu: Writing – original draft, Visualization, Validation, Methodology, Investigation, Formal analysis, Conceptualization. **Johannes Leisen:** Writing – review & editing, Methodology, Investigation. **Yinghao Wen:** Writing – review & editing. **Yixuan Yang:** Writing – review & editing. **Pan Liu:** Writing – review & editing. **Yuanzhi Tang:** Writing – review & editing, Supervision, Project administration, Investigation, Funding acquisition, Conceptualization.

Declaration of competing interest

The authors declare that they have no known competing financial interests or personal relationships that could have appeared to influence the work reported in this paper.

Acknowledgement

This work was supported by the National Science Foundation Grant #2327660. A portion of the measurements were conducted at the Georgia Tech Institute for Matter and Systems, a member of the National Nanotechnology Coordinated Infrastructure (NNCI), which is supported by the National Science Foundation (Grant ECCS-2025462). The authors acknowledge beamline scientists at the National Synchrotron Light Source II (NSLS II) for help with data collection. The authors acknowledge Alicia S. Robang for assistance with NMR numerical simulation.

Appendix A. Supplementary data

Supplementary data to this article can be found online at https://doi.org/10.1016/j.chemgeo.2026.123550.

Data availability

Data are available through Mendeley Data at: DOI:10.17632/2vhsz93n38.1

References

Amiel, N., Dror, I., Berkowitz, B., 2024. Mobility of rare earth elements in coastal aquifer materials under fresh and brackish water conditions. ACS Environ. Au 4 (4), 186–195.
Balaram, V., 2019. Rare earth elements: a review of applications, occurrence, exploration, analysis, recycling, and environmental impact. Geosci. Front. 10 (4), 1285–1303.
Barteková, E., Kemp, R., 2016. National strategies for securing a stable supply of rare earths in different world regions. Res. Policy 49, 153–164.
Bellifemine, Fabio, Poggi, Agostino, Rimassa, Giovanni, 2001. Developing multi-agent systems with JADE, Intelligent Agents VII Agent Theories Architectures and Languages: 7th International Workshop, ATAL 2000 Boston, MA, USA, July 7–9, 2000 Proceedings 7. Springer, pp. 89–103.
Benson, Erin K., Watts, Kathryn E., 2024. Apatite and monazite geochemistry record magmatic and metasomatic processes in rare earth element mineralization at Mountain Pass. Calif. Econ. Geol. 119 (7), 1611–1642.
Borst, Smith, Martin, P., Finch, Adrian A., Estrade, Guillaume, Villanova-de-Benavent, Cristina, Nason, Peter, Marquis, Eva, Horsburgh, Nicola J., Goodenough, Kathryn M., Xu, Cheng, 2020a. Adsorption of rare earth elements in regolith-hosted clay deposits. Nat. Commun. 11 (1), 4386.
Borst, Anouk M., Finch, Adrian A., Friis, Henrik, Horsburgh, Nicola J., Gamaletsos, Platon N., Goettlicher, Joerg, Steininger, Ralph, Geraki, Kalotina, 2020b. Structural state of rare earth elements in eudialyte-group minerals. Mineral. Mag. 84 (1), 19–34.
Boxleiter, Anthony, Elliott, W. Crawford, 2023. Rare-earth minerals in kaolin ore, mine tailings, and sands–Central Georgia, upper coastal plain. Clay Clay Miner. 71 (3), 274–308.
Boxleiter, Anthony, Wen, Yinghao, Tang, Yuanzhi, Elliott, W. Crawford, 2024. Rare-earth element (REE) remobilization and fractionation in bauxite zones from sedimentary kaolin deposits, western Georgia (USA), Upper Coastal Plain. Chem. Geol. 660, 122151.
Boxleiter, Anthony, Wen, Yinghao, Li, Martin Yan Hei, Ashcraft, Joell, Tang, Yuanzhi, Elliott, W. Crawford, 2026. Assessing rare earth (yttrium) speciation in natural ores and processed waste streams using X-ray absorption spectroscopy. Chem. Geol. 707, 123312.
Elderfield, Henry, 1988. The oceanic chemistry of the rare-earth elements. Philos. Trans. R. Soc. London Series A MPS 325 (1583), 105–126.
Elliott, W. Crawford, Gardner, Daniel J., Malla, Prakash, Riley, Ed, 2018. A new look at the occurrences of the rare-earth elements in the Georgia kaolins. Clay Clay Miner. 66 (3), 245–260.
Emsbo, Poul, McLaughlin, Patrick I., du Bray, Edward A., Anderson, Eric D., Vandenbroucke, Thijs R.A., Zielinski, Robert A., 2016. Rare earth elements in sedimentary phosphorite deposits: a global assessment. Rev. Econ. Geol. 18, 101–113.
He, Yilin, Ma, Lingya, Liang, Xiaoliang, Li, Xurui, Zhu, Jianxi, He, Hongping, 2024. Resistant rare earth phosphates as possible sources of environmental dissolved rare earth elements: insights from experimental bio-weathering of xenotime and monazite. Chem. Geol. 661, 122186.
Hossain, M. Khalid, Hossain, Shahadat, Ahmed, Mohammad Hafez, Ishak Md, Khan, Haque, Nazmul, Raihan, Gazi A., 2021. A review on optical applications, prospects, and challenges of rare-earth oxides. ACS Appl. Electron. Mater. 3 (9), 3715–3746.
Huang, Jian, Tan, Wei, Liang, Xiaoliang, He, Hongping, Ma, Lingya, Bao, Zhiwei, Zhu, Jianxi, 2021a. REE fractionation controlled by REE speciation during formation of the Renju regolith-hosted REE deposits in Guangdong Province, South China. Ore Geol. Rev. 134, 104172.
Huang, Yufeng, He, Hongping, Liang, Xiaoliang, Bao, Zhiwei, Tan, Wei, Ma, Lingya, Zhu, Jianxi, Huang, Jian, Wang, Heng, 2021b. Characteristics and genesis of ion adsorption type REE deposits in the weathering crusts of metamorphic rocks in Ningdu, Ganzhou, China. Ore Geol. Rev. 135, 104173.
Hughes, I.D., Däne, M., Ernst, A., Hergert, W., Lüders, M., Poulter, J., Staunton, Julie B., Svane, Axel, Szotek, Z., Temmerman, W.M., 2007. Lanthanide contraction and magnetism in the heavy rare earth elements. Nature 446 (7136), 650–653.
Hunger, Stefan, Cho, Herman, Sims, James T., Sparks, Donald L., 2004. Direct speciation of phosphorus in alum-amended poultry litter: solid-state ^{31}P NMR investigation. Environ. Sci. Technol. 38 (3), 674–681.
Hutchinson, Mandi, Slezak, Paul, Wendlandt, Richard, Hitzman, Murray, 2022. Rare earth element enrichment in the weathering profile of the Bull Hill carbonatite at Bear Lodge, Wyoming, USA. Econ. Geol. 117 (4), 813–831.
Jackson, George A., Williams, Peter M., 1985. Importance of dissolved organic nitrogen and phosphorus to biological nutrient cycling. Deep Sea Res. Part A. Oceanogr. Res. Pap. 32 (2), 223–235.
Jaireth, Subhash, Hoatson, Dean M., Miezitis, Yanis, 2014. Geological setting and resources of the major rare-earth-element deposits in Australia. Ore Geol. Rev. 62, 72–128.
Johannesson, Kevin H., Stetzenbach, Klaus J., Hodge, Vernon F., Lyons, W. Berry, 1996. Rare earth element complexation behavior in circumneutral pH groundwaters: assessing the role of carbonate and phosphate ions. Earth Planet. Sci. Lett. 139 (1–2), 305–319.
Li, Wei, Feng, Xionghan, Yan, Yupeng, Sparks, Donald L., Phillips, Brian L., 2013. Solid-state NMR spectroscopic study of phosphate sorption mechanisms on aluminum (hydr) oxides. Environ. Technol. 47 (15), 8308–8315.
Li, Martin Yan Hei, Zhou, Mei-Fu, Williams-Jones, Anthony E., 2019. The genesis of regolith-hosted heavy rare earth element deposits: insights from the world-class Zudong deposit in Jiangxi Province, South China. Econ. Geol. 114 (3), 541–568.
Li, Martin Yan, Hei, Kwong, Tung, Hiu, Williams-Jones, Anthony E., Zhou, Mei-Fu, 2022. The thermodynamics of rare earth element liberation, mobilization and supergene enrichment during groundwater-regolith interaction. Geochim. Cosmochim. Acta 330, 258–277.
Liu, Pan, Yang, Lufeng, Wang, Qian, Wan, Biao, Ma, Qing, Chen, Hailong, Tang, Yuanzhi, 2020. Speciation transformation of rare earth elements (REEs) during heating and implications for REE behaviors during coal combustion. Int. J. Coal Geol. 219, 103371.
Liu, Pan, Zhao, Simin, Xie, Nan, Yang, Lufeng, Wang, Qian, Wen, Yinghao, Chen, Hailong, Tang, Yuanzhi, 2023. Green approach for rare earth element (REE) recovery from coal fly ash. Environ. Sci. Technol. 57 (13), 5414–5423.
Lookman, R., Grobet, Pierre, Merckx, Roel, Vlassak, Karel, 1994. Phosphate sorption by synthetic amorphous aluminium hydroxides: a 27Al and 31P solid-state MAS NMR spectroscopy study. Eur. J. Soil Sci. 45 (1), 37–44.
Louvel, Marion, Etschmann, Barbara, Guan, Qiushi, Testemale, Denis, Brugger, Joël, 2022. Carbonate complexation enhances hydrothermal transport of rare earth elements in alkaline fluids. Nat. Commun. 13 (1), 1456.
Lozano, Alba, Ayora, Carlos, Macías, Francisco, León, Rafael, Gimeno, María José, Auqué, Luis, 2020. Geochemical behavior of rare earth elements in acid drainages: modeling achievements and limitations. J. Geochem. Explor. 216, 106577.
Mathew, Renny, Gunawidjaja, Philips N., Izquierdo-Barba, Isabel, Jansson, Kjell, García, Ana, Arcos, Daniel, Vallet-Regí, María, Edén, Mattias, 2011. Solid-state ^{31}P and ^{1}H NMR investigations of amorphous and crystalline calcium phosphates grown biomimetically from a mesoporous bioactive glass. J. Phys. Chem. C 115 (42), 20572–20582.
Middleton, Andrew, Hedin, Benjamin C., Hsu-Kim, Heileen, 2024. Recovery of rare earth elements from acid mine drainage with supported liquid membranes: impacts of feedstock composition for extraction performance. Environ. Sci. Technol. 58 (6), 2998–3006.
Miessler, G.L., Fischer, P.J., Tarr, D.A., 2014. Molecular orbitals. In: Inorganic Chemistry, 5th ed. Pearson, Boston, pp. 117–168.
Mitchell, David R.G., 2008. DiffTools: electron diffraction software tools for DigitalMicrograph™. Microsc. Res. Tech. 71 (8), 588–593.
Murphy, J.A.M.E.S., Riley, John P., 1962. A modified single solution method for the determination of phosphate in natural waters. Anal. Chim. Acta 27, 31–36.
Pan, Jiaxin, Zhao, Longsheng, Li, Zheng, Huang, Xiaowei, Feng, Zongyu, Chen, Jun, 2024. Occurrence and vertical distribution of aluminum and rare earths in weathered crust elution-deposited rare earth ore: effect of soil solution pH and clay minerals. J. Rare Earths 42 (7), 1394–1402.
Porvali, Antti, Wilson, Benjamin P., Lundström, Mari, 2018. Lanthanide-alkali double sulfate precipitation from strong sulfuric acid NiMH battery waste leachate. Waste Manag. 71, 381–389.
Poulsen, Søren L., Jakobsen, Hans J., Skibsted, Jørgen, 2010. Incorporation of phosphorus guest ions in the calcium silicate phases of Portland cement from ^{31}P MAS NMR spectroscopy. Inorg. Chem. 49 (12), 5522–5529.
Ravel, Bruce, Newville, M., 2005. ATHENA, ARTEMIS, HEPHAESTUS: data analysis for X-ray absorption spectroscopy using IFEFFIT. Synchrotr. Rad. 12 (4), 537–541.
Ribeiro, Igor Daniel Alves, Volpiano, Camila Gazolla, Vargas, Luciano Kayser, Granada, Camille Eichelberger, Lisboa, Bruno Brito, Passaglia, Luciane Maria Pereira, 2020. Use of mineral weathering bacteria to enhance nutrient availability in crops: a review. Front. Plant Sci. 11, 590774.
Russo, Samantha C., González-Álvarez, Ignacio, Cocker, Helen A., McCoy-West, Alex J., 2025. The fundamentals of rare earth element ion adsorption clay deposits: a mineral systems approach for exploration. J. Geochem. Explor. 278, 107845.
Ruttenberg, Kathleen C., Berner, Robert A., 1993. Authigenic apatite formation and burial in sediments from non-upwelling, continental margin environments. Geochim. Cosmochim. Acta 57 (5), 991–1007.
Ryoo, Ryong, Kim, Jaeheon, Jo, Changbum, Han, Seung Won, Kim, Jeong-Chul, Park, Hongjun, Han, Jongho, Shin, Hye Sun, Shin, Jae Won, 2020. Rare-

earth–platinum alloy nanoparticles in mesoporous zeolite for catalysis. Nature 585 (7824), 221–224.
Sanematsu, Kenzo, Watanabe, Yasushi, 2016. Characteristics and genesis of ion adsorption-type rare earth element deposits. Rev. Econ. Geol. 18, 55–79.
Stumm, Werner, Morgan, James J., 2013. Aquatic Chemistry: Chemical Equilibria and Rates in Natural Waters, 3rd ed. John Wiley & Sons.
Tang, Jianwu, Johannesson, Karen H., 2010. Rare earth elements adsorption onto Carrizo sand: influence of strong solution complexation. Chem. Geol. 279 (3–4), 120–133.
Van Gosen, Bradley S., Verplanck, Philip L., Emsbo, Poul, 2019. Rare Earth Element Mineral Deposits in the United States. US Geological Survey.
Veshtort, Mikhail, Griffin, Robert G., 2006. SPINEVOLUTION: a powerful tool for the simulation of solid and liquid state NMR experiments. J. Magn. Reson. 178 (2), 248–282.
Wen, Yinghao, Hu, Lei, Boxleiter, Anthony, Li, Dien, Tang, Yuanzhi, 2023. Rare earth elements recovery and waste management of municipal solid waste incineration ash. ACS Sustain. Resour. Manage. 1 (1), 17–27.
Wood, Scott A., 1990. The aqueous geochemistry of the rare-earth elements and yttrium: 1. Review of available low-temperature data for inorganic complexes and the inorganic REE speciation of natural waters. Chem. Geol. 82, 159–186.
Wu, Zhenxiao, Chen, Yu, Wang, Yang, Xu, Yuan, Lin, Zhuoling, Liang, Xiaoliang, Cheng, Hongfei, 2023. Review of rare earth element (REE) adsorption on and desorption from clay minerals: application to formation and mining of ion-adsorption REE deposits. Ore Geol. Rev. 157, 105446.
Wu, Zengxue, Liu, Jingjing, Li, Chun, Liu, Wei, Wu, Weixiang, 2025. Redistribution and enhanced bioavailability of rare earth elements speciation induced by mining-driven transformation in ionic rare earth mining areas. Sci. Rep. 15 (1), 27345.
Xu, Hang, Leisen, Johannes, Robang, Alicia S., Wen, Yinghao, Wan, Biao, Zhao, Simin, Paravastu, Anant, Phillips, Brian L., Tang, Yuanzhi, 2025. Phosphate effects on rare earth element sorption onto kaolinite: molecular-scale insights at circumneutral pH. Geochim. Cosmochim. Acta 408, 132–143.